Supplementary Material for 'A Unified Thermal Transport Picture Across Phases Via Spatiotemporal Coherence'

Zhongwei Zhang,[1] Yangyu Guo,[2] Marc Bescond,[3] Peter Hänggi,[4,5] Sebastian Volz,[6,7,*] and Jie Chen[1,†]

[1] *Center for Phononics and Thermal Energy Science, China-EU Joint Lab for Nanophononics, MOE Key Laboratory of Advanced Micro-structured Materials, School of Physics Science and Engineering, Tongji University, Shanghai 200092, People's Republic of China*

[2] *Institut Lumière Matière, Université Claude Bernard Lyon 1-CNRS, Université de Lyon, Villeurbanne 69622, France*

[3] *IM2NP, UMR CNRS 7334, Aix-Marseille Université, Faculté des Sciences de Saint Jérôme, Case 142, 13397 Marseille Cedex 20, France*

[4] *Institute of Physics, University of Augsburg, 86135 Augsburg, Germany*

[5] *Max Planck Institute for the Physics of Complex Systems, Nöthnitzer Strasse 38, D-01187 Dresden, Germany*

[6] *Center for Phononics and Thermal Energy Science, China-EU Joint Lab for Nanophononics, MOE Key Laboratory ofAdvanced Micro-structured Materials, School of Physics Science and Engineering, Tongji University, Shanghai 200092, People's Republic of China*

[7] *Laboratory for Integrated Micro and Mechatronic Systems, CNRS-IIS UMI 2820, The University of Tokyo, Tokyo 153-8505, Japan*

S1. MD simulation details

S1.1. *Ab initio* MD simulations

The VASP code [1–3] is used with potpaw-PBE.54 [4] pseudopotentials to perform *ab initio* molecular dynamic (AIMD) simulations to collect the energies, atomic force, and stress as datasets for the training of the machine learning based neuroevolution potential (NEP). The system of water for AIMD calculations contains 180 molecules with 360 atoms. The cutoff energy of 400 eV is used. A 3×3×3 Γ-centered grid of k points in the irreducible Brillouin zone is used. To fully consider the effect of temperature on phase transition, AIMD is performed in the isothermal-isobaric (NPT) ensemble at the temperatures of 50 K, 100 K, 300 K, 500 K, 600 K, 700 K and 1000 K. The time step is 0.25 fs. The 12000 and 5000 AIMD atomic configurations and the corresponding atomic forces, total energies, and stresses are used to train and test NEP potential, respectively.

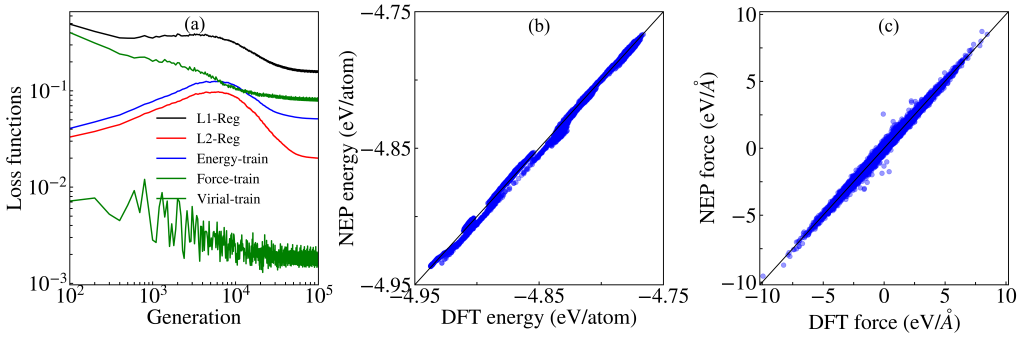

FIG. S1. (a) Evolution of the loss functions for L1-regression, L2-regression, energy, force, and virial during the training process. (b) The comparison of potential energy between DFT calculations and NEP based predictions for the test set. (b) The comparison of atomic forces between DFT calculations and NEP based predictions for the test set.

* Corresponding: volz@iis.u-tokyo.ac.jp
† Corresponding: jie@tongji.edu.cn

S1.2. Machine learning potential

We employ a NEP potential developed by Fan et al. [5] as a machine learning potential model to describe the complex interactions between and inside the water molecules. With the trained NEP, we would be able to do further lattice dynamic and molecular dynamic calculations by using the GPUMD software [6]. To begin with, the trained NEP is tested by comparing the energies and atomic forces predicted by DFT and NEP predictions, which reveals a good agreement between the two calculations (See Fig. S1).

S1.3. Direct MD simulations

All MD simulations are carried out using the LAMMPS [7] and GPUMD [6] packages with a time step of 0.25 fs. LAMMPS is performed with the TIP4P model [8] and GPUMD with the NEP model. The system of water for MD calculations containing 2000 molecules with 6000 atoms is used for our MD simulations, ensuring that size effects are eliminated. After the structure relaxation and thermal equilibration in the isothermal-isobaric (NPT) ensemble under atmosphere pressure for 750 ps, EMD simulations with the microcanonical (NVE) ensemble are performed to record the atomic trajectories. A simulation time of 3 ns is used for the thermal conductivity calculations which is sufficient to ensure the convergence. Note that systems for different phases considered in our work all have zero net velocities. To account for statistical fluctuations, the final results are averaged over five independent simulations.

S2. Phase diagram of water

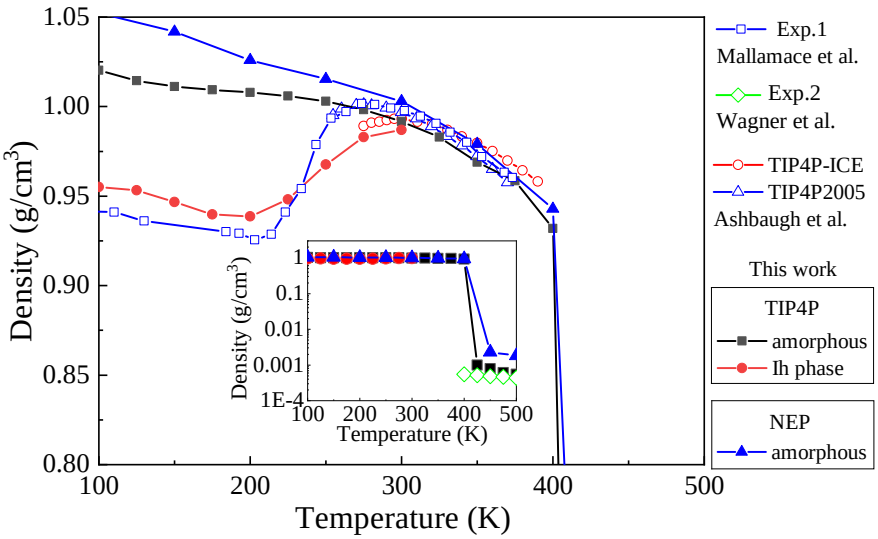

FIG. S2. Phase diagram of water in terms of mass density vs temperature at ambient pressure from our calculations and previous reports. Experimental data are from Mallamace et al. [9] and Wagner et al. [10], while the simulation results with TIP4P-ICE and TIP4P/2005 potential are taken from [11]. The inset highlights the gas-phase region.

Accurate reproduction of the phase diagram provides a critical test for the physical validity of an empirical potential, particularly when investigating phase-dependent properties. The phase diagram in Fig. S2 shows that the TIP4P and NEP potentials used in this work correctly capture water phase transitions. The distribution of the amorphous state across the full temperature range is well represented, covering solid, liquid, and gas phases. Furthermore, the simulation results agree closely with experimental data [9, 10] and previous simulations [11]. In particular, the results reproduce the extremely low density of water vapor at 1 atm in the gas phase above 400 K. These findings confirm that our MD simulations, based on the employed empirical model, accurately reproduce the phase behavior of water, thereby providing a crucial foundation for the subsequent analysis of thermal transport.

S3. Methodologies

S3.1. Our analytical workflow

Our research follows a clear logical progression, with each analytical approach providing complementary insights. Figure S3 provides a schematic overview of the methods used and their logical progression.

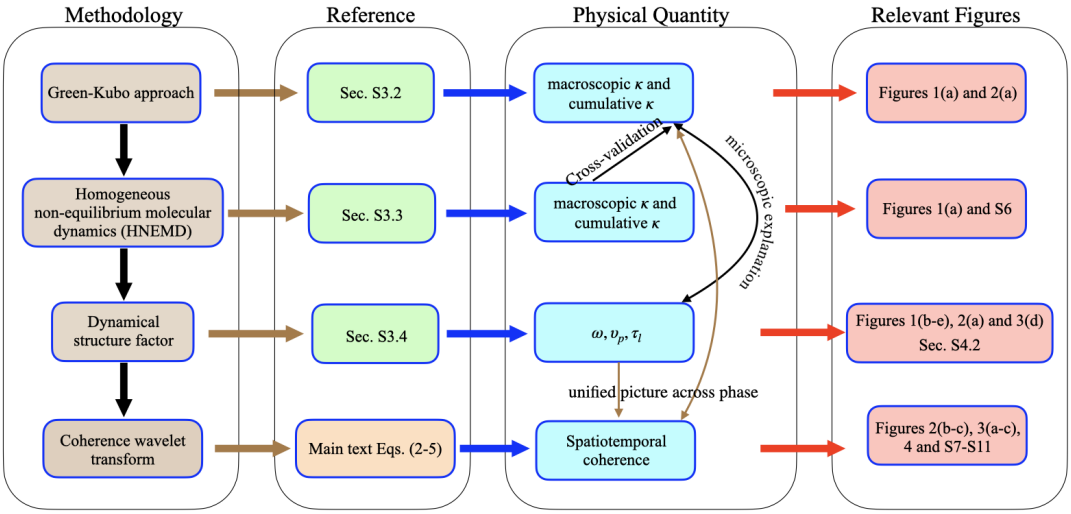

FIG. S3. Schematic figure of the methodologies used in this work and their logical progression.

We first use the equilibrium Green-Kubo (GK) method to calculate the macroscopic κ. This provides a macroscopic foundation, allowing us to distinguish between conduction and convection contributions, and laying the groundwork for our subsequent microscopic analysis (results in Figures 1(a) and 2(a)). To reveal the underlying physical mechanisms, we use three complementary methods:

- Dynamic structure factor (DSF) analysis is used to study the modal properties of thermal vibrations, including frequency ω, and propagation velocity v_p (results in Figures 1(b-e), 2(a), and 3(d)).
- Homogeneous non-equilibrium molecular dynamics (HNEMD) is employed to corroborate the GK and DSF results shown in Figures 1(a) and 2(a), particularly in characterizing the significant contribution of low-frequency transverse modes to κ in the liquid-gas transition phase (results in Figure S6).
- Temporal wavelet transform is used to investigate the spatiotemporal coherence of heat transport, providing a direct microscopic image of thermal transport across phases (results in Figures 2(b-c) and (3)).

S3.2. Green-Kubo calculations

The thermal conductivity κ can be evaluated via the Green-Kubo approach with the autocorrelation of the heat flux $\mathbf{J}(t)$:

$$\kappa = \frac{1}{3k_B T^2 V} \int \langle \mathbf{J}(t) \cdot \mathbf{J}(0) \rangle \, dt, \tag{S1}$$

where V corresponds to the system volume. k_B and T denote the Boltzmann constant and temperature, respectively. $\mathbf{J}(t)$ can be defined from atomic properties as

$$\mathbf{J}(t) = \sum_i E_i(t) \mathbf{v}_i(t) - \sum_i \mathbf{S}_i(t) \mathbf{v}_i(t), \tag{S2}$$

where E_i, $\mathbf{v}_i$ and $\mathbf{S}_i$, respectively, correspond to the total energy, velocity and stress of i-th atom. The first term represents diffusion-driven convection, while the second-term encompasses the conduction-based contribution.

The Green-Kubo calculations are based on equilibrium molecular dynamics (EMD) simulations, which are carried out using the LAMMPS package [7] with the TIP4P model [8]. A system of 2000 water molecules (6000 atoms) is used for our simulations. After structural relaxation and thermal equilibration in the isothermal-isobaric (NPT) ensemble under atmospheric pressure for 750 ps with a time step of 0.25 fs, EMD simulations with the microcanonical (NVE) ensemble are performed to record the heat flux $\mathbf{J}(t)$. A simulation time of 3 ns is used for the κ calculations, which is sufficient to ensure convergence. To account for statistical fluctuations, the final results are averaged over five independent simulations.

Building upon the Green-Kubo formalism, we extended its application to predict the modal thermal conductivities of our system. Prior work by Gill-Comeau *et al.* [12] and Lv *et al.* [13] calculated modal thermal conductivities by projecting heat flux onto normal modes, which is suitable for solids. However, to investigate thermal transport in disordered phases like liquids and gases, we move beyond the conventional phonon picture. Accordingly, we have advanced this methodology by projecting the heat flux onto a basis of collective excitations (see Section S2.4 for this concept). This approach allows us to define the heat flux at a quasi-wavevector, i.e. $\mathbf{J}_{\mathbf{k}}(t)$, as follows

$$\mathbf{J}_{\mathbf{k}}(t) = \sum_i E_i(t)\,\mathbf{v}_i(t)\,e^{i\mathbf{k}\cdot\mathbf{r}_i(t)} - \sum_i \mathbf{S}_i(t)\,\mathbf{v}_i(t)\,e^{i\mathbf{k}\cdot\mathbf{r}_i(t)}. \tag{S3}$$

Using this modal heat flux, the thermal conductivity at mode level $\kappa_{\mathbf{k}}$ can be further estimated from the Green-Kubo approach:

$$\kappa_{\mathbf{k}} = \mathrm{Re}\frac{V}{3k_BT^2}\int \langle \mathbf{J}_{\mathbf{k}}(t)\cdot\mathbf{J}^*_{\mathbf{k}}(0)\rangle\, dt. \tag{S4}$$

$*$ denotes the conjugate of a complex. By leveraging the frequency-wavevector relationship obtained from DSF, we can derive the frequency-dependent thermal conductivity, i.e. $\kappa(\omega)$. This ultimately allows us to predict cumulative thermal conductivity $\kappa \equiv \int_0^\omega \kappa(\omega')\,d\omega'$, and to quantify the distinct contributions from various polarization and frequency components across different phases.

S3.3. Homogeneous nonequilibrium molecular dynamics

We also used the HNEMD method [14] to compute the κ of the water system for the cross-validation of results from GK and DSF analysis. This method has been widely used to investigate the thermal properties of bulk materials. The simulations are performed using the GPUMD package [6] with the NEP model [5]. A detailed description and data of the training and simulation of the NEP potential are freely available at https://github.com/ZhongweiZhangsite/NEP-water-phase-transition. Note that the NEP potential shows discrepancies in predicting structural information [15], such as pair distribution functions, whereas it reliably reproduces the κ and related dynamic behaviors of water systems. Periodic boundary conditions are applied in all directions. The water system is first equilibrated in NPT and NVT ensembles at 300 K for 1 ns, respectively. In the HNEMD simulations, an external driving force (with zero net force) is added to the atoms in the system, leading to a heat flux that has a nonzero ensemble average. In the linear-response regime, the heat current $\mathbf{J}$ is proportional to the driving force parameter $\mathbf{F}_e$:

$$\langle J^\alpha\rangle = TV\sum_\beta \kappa^{\alpha\beta}F_e^\beta, \tag{S5}$$

where T is the temperature and V is the volume of the system. $\langle\rangle$ indicates the ensemble average over time. The magnitude of the driving force parameter is tested and chosen as $F_e^x = 4\times10^{-5}$ Å^{-1} along x direction. A production run of 10 ns and 5 independent simulations are used, which is long enough to ensure convergence.

Moreover, the HNEMD method is employed to cross-validate the significant contribution of low-frequency transverse modes to κ, which is also revealed by the DSF analysis. As developed by Fan *et al.* [14], the steady-state correlation function of time $K(t)$ is defined as:

$$K(t) = \sum_i\sum_{j\neq i}\mathbf{r}_{ij}(0)\left\langle \frac{\partial U_j}{\partial \mathbf{r}_{ji}}(0)\cdot\frac{\mathbf{p}_i(t)}{m_i}\right\rangle_{\mathrm{ne}}, \tag{S6}$$

which reduces to the nonequilibrium heat current (the potential part $\mathbf{p}_i(t)$) when $t = 0$. For simplicity, we will only work with a diagonal component of the thermal conductivity tensor and drop the tensorial notations. The spectral thermal conductivity is then obtained via Fourier transform:

$$\kappa(\omega) = \frac{2}{TVF_e}\int_{-\infty}^{\infty} dt e^{i\omega t} K(t). \tag{S7}$$

This spectral decomposition method can be used to study the microscopic thermal transport mechanisms in the diffusive regime of a bulk water system. Furthermore, to gain insight into the polarization dependence of spectral κ, we adapt a concept developed by Fan *et al.* [16], which decomposes the contributions into in-plane and out-of-plane modes for two-dimensional materials. In our three-dimensional water system, the out-of-plane polarization correspond to the transverse polarization, which are polarized perpendicular to the transport direction (i.e., the applied F_e^x direction). In contrast, the in-plane polarizations represent the degenerate transverse and longitudinal components in a three-dimensional system. Following this concept, we rewrite the steady-state correlation function to obtain contributions from longitudinal (i.e. Lg) and transverse (i.e. Tr) polarizations:

$$K_{Lg}(t) = \sum_i \sum_{j\neq i} \mathbf{r}_{ij}(0) \left\langle \frac{\partial U_j}{\partial x_{ji}}(0) \cdot \frac{p_i^x(t)}{m_i} \right\rangle_{\text{ne}}, \tag{S8}$$

$$K_{Tr}(t) = \sum_i \sum_{j\neq i} \mathbf{r}_{ij}(0) \left(\left\langle \frac{\partial U_j}{\partial y_{ji}}(0) \cdot \frac{p_i^y(t)}{m_i} \right\rangle_{\text{ne}} + \left\langle \frac{\partial U_j}{\partial z_{ji}}(0) \cdot \frac{p_i^z(t)}{m_i}. \right\rangle_{\text{ne}} \right) \tag{S9}$$

By further performing the Fourier transform as Eq. S7, we can further calculate the spectral κ and also the cumulative κ to cross-validate our predictions based on the Green-Kubo approach and also DSF analysis.

Moreover, in TABLE S1, we compare the thermal conductivities of different phases obtained from various approaches. The values are in close agreement, indicating solid cross-validation of the adopted methods and the high accuracy of our predictions.

TABLE S1. The thermal conductivities of different phases obtained from different approaches. All the results are in the unit of $\mathrm{Wm^{-1}K^{-1}}$

	Solid (100 K)	**Liquid (300 K))**	**Trans. liquid/gas (400 K)**	**Gas (500 K)**
GK	1.86±0.17	1.32±0.09	1.67±0.10	1.28±0.15
Modal GK	1.83±0.15	1.22±0.08	1.69±0.09	1.24±0.15
HNEMD	1.14±0.25	0.86±0.20	1.04±0.16	0.86±0.11
Modal HNEMD	1.20±0.26	0.88±0.21	1.05±0.17	0.88±0.10

S3.4. Dynamical structure factor

By treating the thermal vibrations as collective excitations, the vibrations in disordered materials can be studied via the dynamical structure factor (DSF). The longitudinal and transverse DSF, $\mathrm{DSF}_{Lg}(\mathbf{k},\omega)$ and $\mathrm{DSF}_{Tr}(\mathbf{k},\omega)$, are respectively given as [17, 18]

$$\mathrm{DSF}_s(\mathbf{k},\omega) = \frac{|\mathbf{k}|^2}{2\pi\omega^2}\int dt \,\langle \mathrm{u}_s(\mathbf{k},t)\mathrm{u}_s(-\mathbf{k},t)\rangle e^{i\omega t}, \tag{S10}$$

where s can be the longitudinal (Lg) or the transverse (Tr) polarization. $\mathbf{k}$ refers to the quasi-wavevector and ω to the angular frequency. The time t dependent collective velocity $\mathrm{u}_s(\mathbf{k},t)$ can be further expressed as

$$\mathrm{u}_{Lg}(\mathbf{k},t) = \frac{1}{N}\sum_i \sqrt{m_i} v_{i,x}(t)\, e^{i\mathbf{k}\cdot\mathbf{r}_i(t)}, \tag{S11}$$

$$\mathrm{u}_{Tr}\left(\mathbf{k},t\right)=\frac{1}{2N}\sum_{i}\sqrt{m_i}\left(v_{i,y}\left(t\right)+v_{i,z}\left(t\right)\right)e^{i\mathbf{k}\cdot\mathbf{r}_i(t)}, \tag{S12}$$

where $\mathbf{k}$ only set in the k_x direction in our calculations. $\mathbf{r}_i$ refers to the atomic position of the i-th atom. $v_{i,x}$, $v_{i,y}$, $v_{i,z}$ are the velocity components of the i-th atom along the x, y, z Cartesian directions. N denotes the total number of atoms. Compared to previous works [19–22], we introduced an atomic mass term in the equations to account for the binary mass of atoms in water, which is crucial for accurate analysis of collective vibrations. The atomic information of $\mathbf{v}_i\left(t\right)$ and $\mathbf{r}_i\left(t\right)$ can be calculated from MD simulations of the water systems across different phases. The collective displacement for visualizing real-space atomic motions can be obtained by replacing the atomic velocity with displacement and removing the mass term in Eqs. (S11-S12).

S4. Thermal vibrational and transport properties

S4.1. Thermal conductivity of liquids

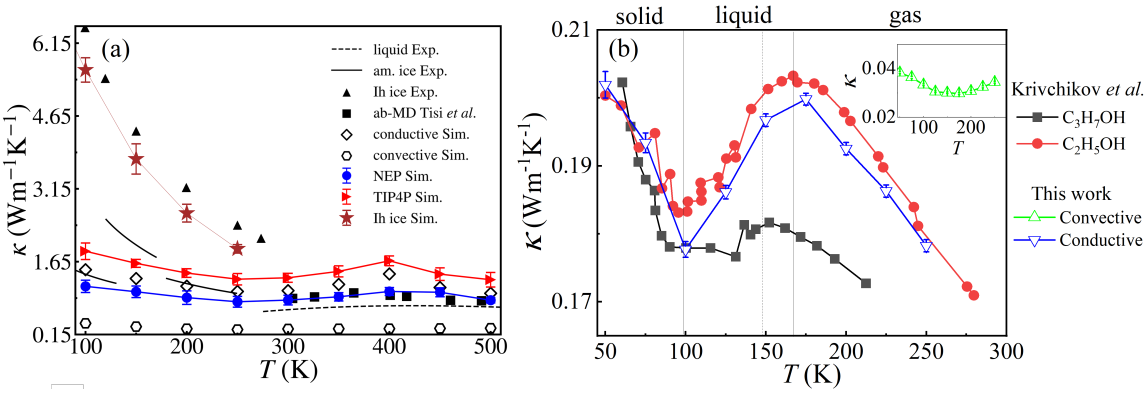

FIG. S4. (a) Thermal conductivities of water across different phases. (b) Thermal conductivities of C_3H_7OH and C_2H_5OH, with reported results (filled symbols) from Ref. [25]. The predicted values in this work (open symbols) are obtained from molecular dynamics (MD) simulations using the Green–Kubo approach with an empirical potential from Ref. [25]. The inset in (b) shows the convective contribution to κ.

In Figure S4(a), the temperature-dependent thermal conductivity of Ih crystalline ice is shown, with calculated κ matching experimental measurements, confirming both the decreasing trend of κ with temperature in solids and the accuracy of the TIP4P model for water interactions during phase transitions.

Figure S4(b) presents temperature-dependent thermal conductivities of propanol (C_3H_7OH) and ethanol (C_2H_5OH) [25]. Both materials exhibit a non-monotonic change in κ, first decreasing in the solid phase, then increasing in the liquid phase, and finally decreasing again as they transition to the gas phase. This behavior is remarkably similar to that observed in the water system discussed in the main text, highlighting that the observed complex κ trend is a general phenomenon driven by the changes in atomic and vibrational transport mechanisms.

S4.2. Longitudinal thermal vibrations across phases

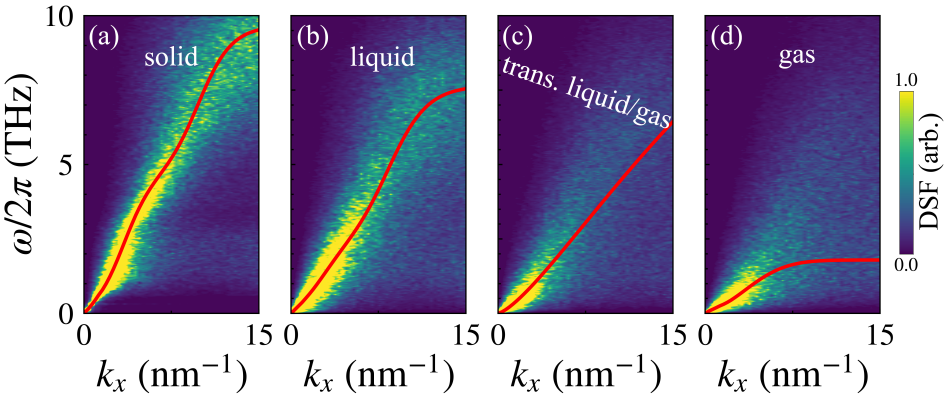

FIG. S5. DSF of longitudinal polarization of water at different phases, i.e., am. solid (100 K), liquid (300 K), trans. liquid/gas (400 K) and gas (500 K).

In Figures S5, longitudinal thermal vibration frequencies decrease with temperature, and line broadening indicates reduced lifetimes during phase transitions, consistent with transverse modes discussed earlier. Despite significant liquid-like modes in transverse polarization, longitudinal vibrations in Figs. S5 maintain strong phonon-like behavior.

S4.3. Thermal conductivity from HNEMD approach

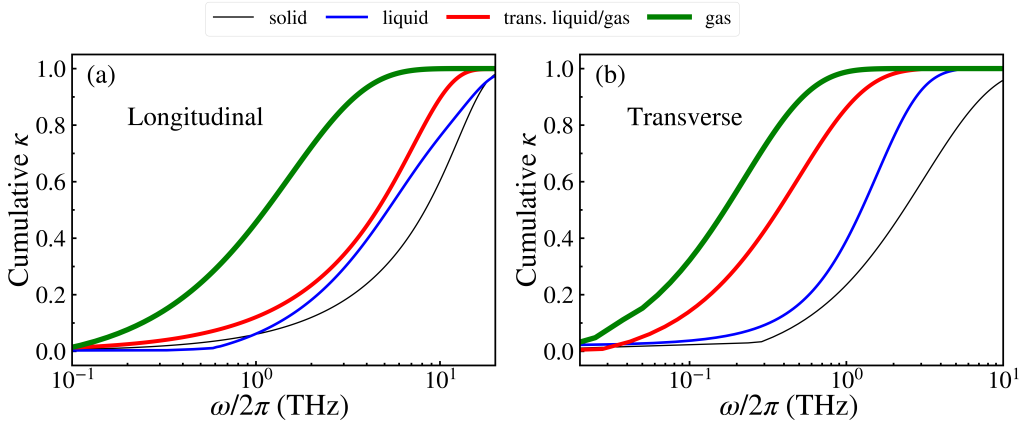

FIG. S6. The cumulative thermal conductivity (κ) of water across phases for (a) longitudinal and (b) transverse polarizations.

Figure S6 displays the cumulative thermal conductivity (κ) of water across phases, derived using homogeneous nonequilibrium molecular dynamics (HNEMD) with the NEP model. It highlights the significant contributions of low-frequency transverse modes during phase transitions to trans. liquid/gas and gas.

S5. Coherence of thermal vibrations

S5.1. Coherence time for transverse modes

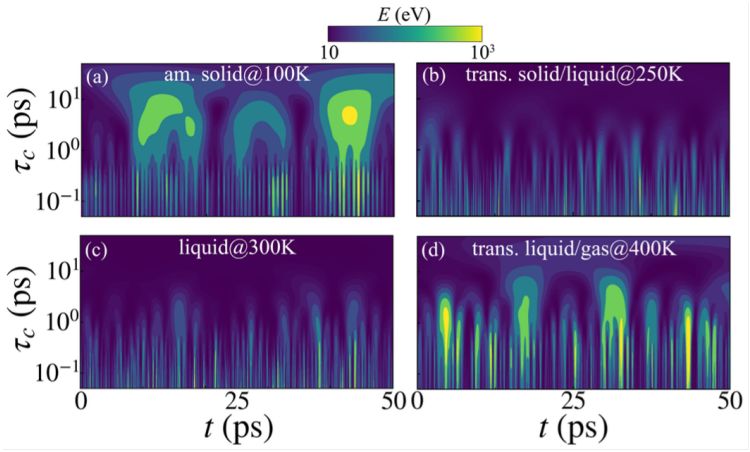

FIG. S7. Evolution-time- and coherence-time-dependent energy (color scale) of water across (a) am. solid at 100K, (b) trans. solid/liquid at 250K, (c) liquid at 300K and (d) trans. liquid/gas at 400K for Tr modes at quasi-wavevector 3.0 nm^{-1}.

S5.2. Coherence time for longitudinal modes

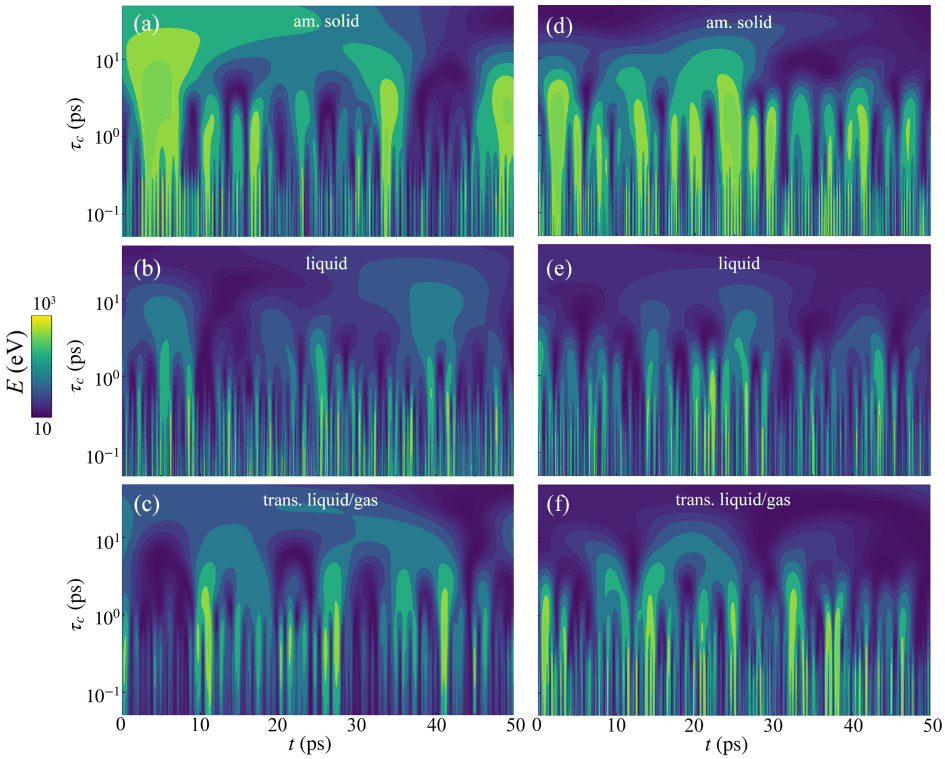

FIG. S8. Evolution-time- and coherence-time-dependent energy (color scale) of water across different phases for (a-c) the longitudinal mode at quasi-wavevector 3.0 nm^{-1}, and (d-f) the transverse mode at quasi-wavevector 10.0 nm^{-1}.

S5.3. The coherence delay of decay

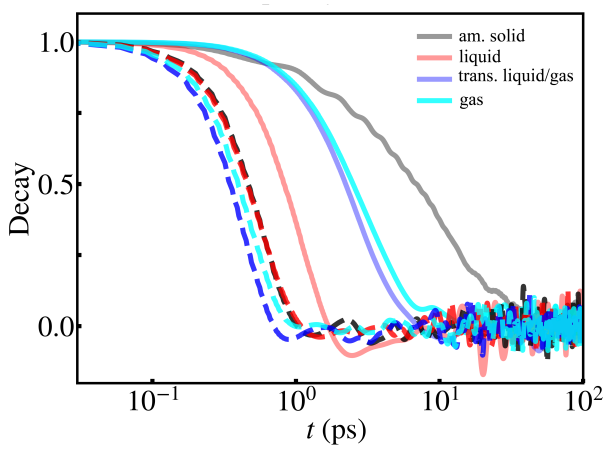

FIG. S9. Decay of low-frequency thermal vibrations across phases at wavevector 3.0 nm^{-1}, with solid and dashed lines representing transverse and longitudinal polarizations, respectively.

S5.4. Variation in gas phase

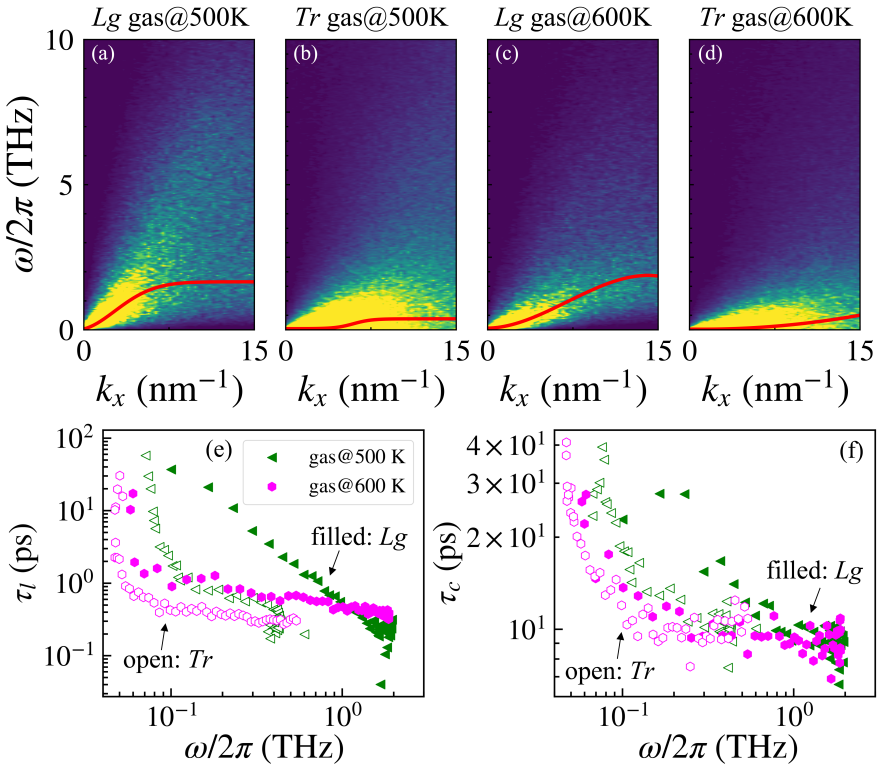

FIG. S10. (a–d) Longitudinal and transverse polarizations of the dynamic structure factor (DSF) of water in the gas phase at 500 K and 600 K, respectively. The red lines indicate the center frequencies of the DSF at different quasi-wavevectors, while the color scale represents the DSF intensity normalized to its maximum value. (e) Lifetime (τ_l) and (f) coherence time (τ_c) of water in the gas phase at 500 K and 600 K.

The dynamical structure factor in the Figs. S10(a-d) shows that as increasing temperature from 500 K to 600 K in the gas phase, the thermal vibrations further been suppressed to low-frequencies. In addition, as shown in Figs.

S10(e-f), the lifetime and coherence time is also further decreasing with the temperature in the gas phase. Both the declined vibrational frequency and coherence time are consistent well with the decreasing of κ with temperature in gas phase.

S5.5. Spatial coherence

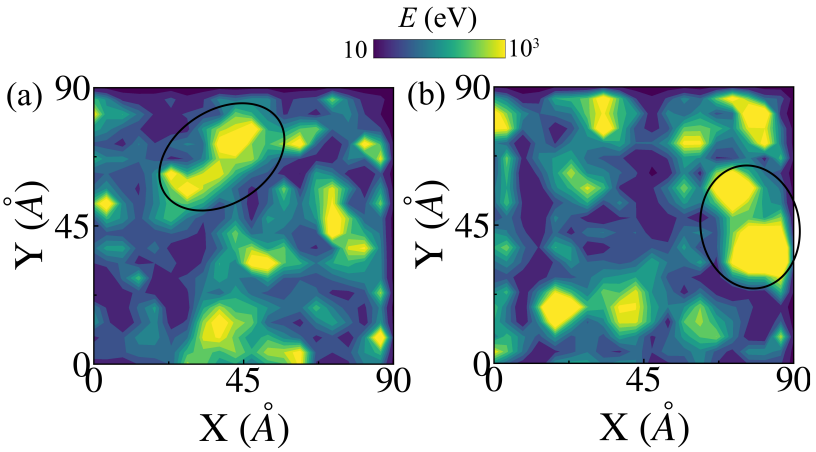

FIG. S11. Two temporal snapshots of the spatially (X-Y) plane projection of energy (color level) of the Ih phase of solid ice for the (a) Tr and (b) Lg modes at the quasi-wavevector of 3.0 nm^{-1}.

S6. The generation of coherence across phases

Treating the atomic diffusion velocity as υ_d and the averaged distance between vibrational wavepackets as d, the averaged collision time τ_{col} between different wavepackets yields

$$\tau_{col} = \frac{d}{\upsilon_d}. \tag{S13}$$

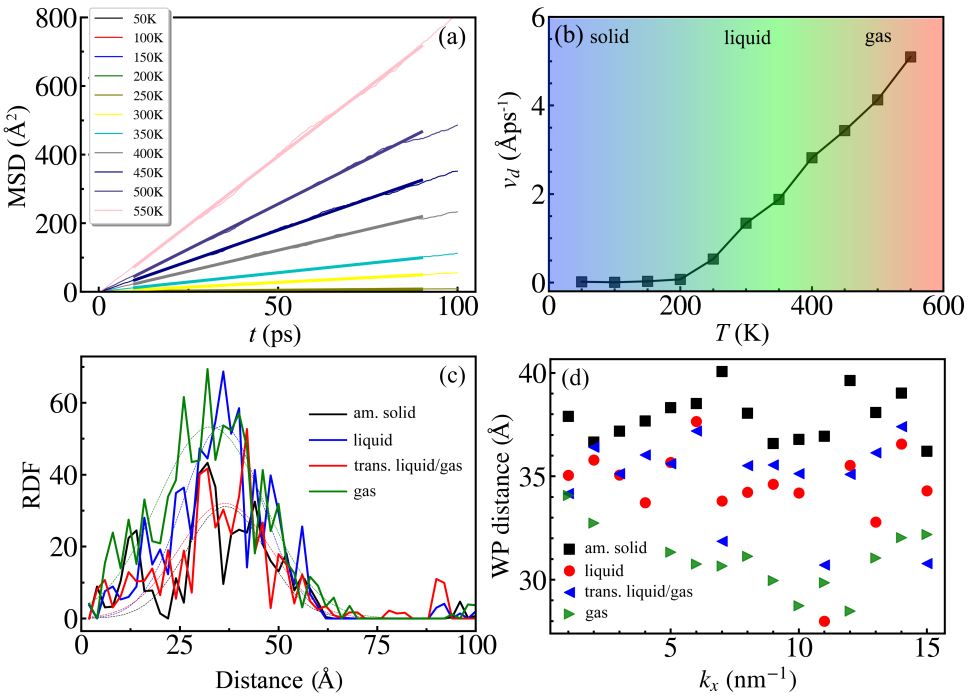

FIG. S12. (a) Temperature-dependent mean square displacement (MSD) of water. (b) Diffusion velocity (v_d) of water versus temperature. (c) Radial distribution function (RDF) of water at various temperatures for the low-frequency mode at quasi-wavevector 3.0 nm^{-1}. (d) Average wavepacket (WP) distance for different modes at various wavevectors.

The mean square displacement (MSD) obtained from direct MD simulations describes atomic motion, calculated as:

$$\mathrm{MSD}\,(t) = \left\langle \left|\mathbf{r}\,(t) - \mathbf{r}_0\right|^2 \right\rangle, \tag{S14}$$

where $\mathbf{r}_0$ is the initial position. The self-diffusion coefficient D is then estimated by fitting the MSD curve (Fig. S13(a)), showing significant phase dependence (Fig. S13(b)). Using D, the atomic diffusion velocity v_d is calculated as $v_d = \sqrt{6D/t}$.

The wavelet transform approach provides spatial thermal energy distribution for a specific mode, revealing the distance between thermal vibration wavepackets. The radial distribution function (RDF) of spatial thermal energy estimates average wavepacket distances. In Fig. S13(c), RDF for a specific mode at quasi-wavevector 3.0 nm^{-1} shows weak temperature dependence. Further calculation of wavepacket distances (d) across the spectrum (Fig. S13(d)) reveals d to be independent of both modes and temperature (i.e., across different disordered phases). This letter adopts an average d value of 35 $\mathring{A}$.

S6.1. The spatial vibrations

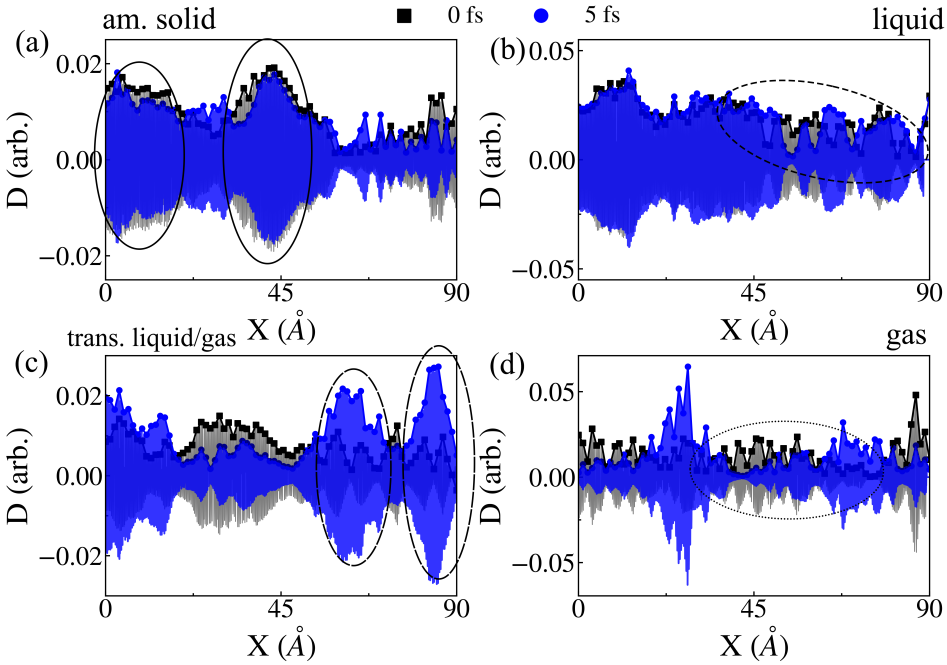

FIG. S13. (a–d) Snapshots of the real-space atomic displacements along the X direction for isotropic water across different phases, for the transverse (Tr) mode at a quasi-wavevector of 3.0 nm^{-1}. Circles highlight the distinct behaviors of vibrational delocalization and correlation in different phases.

[1] G. Kresse and J. Hafner, Ab initio molecular dynamics for liquid metals, Phys. Rev. B **47**, 558 (1993).
[2] G. Kresse and J. Furthmüller, Efficient iterative schemes for ab initio total-energy calculations using a plane-wave basis set, Phys. Rev. B **54**, 11169 (1996).
[3] G. Kresse and J. Furthmüller, Efficiency of ab-initio total energy calculations for metals and semiconductors using a plane-wave basis set, Comput. Mater. Sci. **6**, 15 (1996).
[4] G. Kresse and J. Hafner, Norm-conserving and ultrasoft pseudopotentials for first-row and transition elements, J. Condens. Matter Phys. **6**, 8245 (1994).
[5] Z. Fan, Z. Zeng, C. Zhang, Y. Wang, K. Song, H. Dong, Y. Chen, and T. Ala-Nissila, Neuroevolution machine learning potentials: Combining high accuracy and low cost in atomistic simulations and application to heat transport, Phys. Rev. B **104**, 10.1103/PhysRevB.104.104309 (2021).
[6] Z. Fan, W. Chen, V. Vierimaa, and A. Harju, Efficient molecular dynamics simulations with many-body potentials on graphics processing units, Comput. Phys. Commun. **218**, 10 (2017).
[7] S. Plimpton, Fast Parallel Algorithms for Short-Range Molecular Dynamics, J. Comput. Phys. **117**, 1 (1995).
[8] W. L. Jorgensen, J. Chandrasekhar, J. D. Madura, R. W. Impey, and M. L. Klein, Comparison of simple potential functions for simulating liquid water, J. Chem. Phys. **79**, 926 (1983).
[9] F. Mallamace, C. Branca, M. Broccio, C. Corsaro, C.-Y. Mou, and S.-H. Chen, The anomalous behavior of the density of water in the range 30 K $< T <$ 373 K, Proceedings of the National Academy of Sciences **104**, 18387 (2007).
[10] W. Wagner and A. Pruß, The iapws formulation 1995 for the thermodynamic properties of ordinary water substance for general and scientific use, Journal of Physical and Chemical Reference Data **31**, 387 (2002).
[11] H. S. Ashbaugh, N. J. Collett, H. W. Hatch, and J. A. Staton, Assessing the thermodynamic signatures of hydrophobic hydration for several common water models, The Journal of Chemical Physics **132**, 124504 (2010).
[12] M. Gill-Comeau and L. J. Lewis, Heat conductivity in graphene and related materials: A time-domain modal analysis, Phys. Rev. B **92**, 195404 (2015).
[13] W. Lv and A. Henry, Direct calculation of modal contributions to thermal conductivity via Green–Kubo modal analysis, New Journal of Physics **18**, 013028 (2016).

[14] Z. Fan, H. Dong, A. Harju, and T. Ala-Nissila, Homogeneous nonequilibrium molecular dynamics method for heat transport and spectral decomposition with many-body potentials, Physical Review B **99**, 064308 (2019).
[15] Z. Chen, M. L. Berrens, K.-T. Chan, Z. Fan, and D. Donadio, Thermodynamics of Water and Ice from a Fast and Scalable First-Principles Neuroevolution Potential, Journal of Chemical & Engineering Data **69**, 128 (2024).
[16] Z. Fan, L. F. C. Pereira, P. Hirvonen, M. M. Ervasti, K. R. Elder, D. Donadio, T. Ala-Nissila, and A. Harju, Thermal conductivity decomposition in two-dimensional materials: Application to graphene, Phys. Rev. B **95**, 10.1103/PhysRevB.95.144309 (2017).
[17] J. P. Boon and S. Yip, *Molecular hydrodynamics* (Courier Corporation, 1991).
[18] H. Shintani and H. Tanaka, Universal link between the boson peak and transverse phonons in glass, Nature Materials **7**, 870 (2008).
[19] R. M. Khusnutdinoff, C. Cockrell, O. A. Dicks, A. C. S. Jensen, M. D. Le, L. Wang, M. T. Dove, A. V. Mokshin, V. V. Brazhkin, and K. Trachenko, Collective modes and gapped momentum states in liquid Ga: Experiment, theory, and simulation, Physical Review B **101**, 214312 (2020).
[20] H. Ohta and S. Hamaguchi, Wave Dispersion Relations in Yukawa Fluids, Physical Review Letters **84**, 6026 (2000).
[21] J.-D. Chai, D. Stroud, J. Hafner, and G. Kresse, Dynamic structure factor of liquid and amorphous Ge from *ab initio* simulations, Physical Review B **67**, 104205 (2003).
[22] Y. Xu, X. Xiang, Z. Li, and Y. Zhou, Microscopic dynamics of collective acoustic excitations in simple liquids, Physical Review B **111**, 174208 (2025).
[23] The code providing the calculation of phonon coherence and coherence corrected thermal conductivity according to our model as an open-source package, WPPT, in https://github.com/ZhongweiZhangsite/WPPT.
[24] Z. Zhang, Y. Guo, M. Bescond, J. Chen, M. Nomura, and S. Volz, Generalized decay law for particlelike and wavelike thermal phonons, Phys. Rev. B **103**, 184307 (2021).
[25] A. I. Krivchikov, A. N. Yushchenko, O. A. Korolyuk, F. J. Bermejo, C. Cabrillo, and M. A. González, Anomaly in temperature dependence of thermal transport of two hydrogen-bonded glass-forming liquids, Phys. Rev. B **75**, 214204 (2007).
[26] J. Tersoff, New empirical approach for the structure and energy of covalent systems, Phys. Rev. B **37**, 6991 (1988).
[27] M. L. Huber, R. A. Perkins, D. G. Friend, J. V. Sengers, M. J. Assael, I. N. Metaxa, K. Miyagawa, R. Hellmann, and E. Vogel, New international formulation for the thermal conductivity of h2o, Journal of Physical and Chemical Reference Data **41**, 033102 (2012).